



## Regulation the reactive oxygen species on conjugated polymers for highly efficient photocatalysis

Huijie Yan<sup>a</sup>, Yanchun Deng<sup>b</sup>, Minhui Shen<sup>a</sup>, Yu-Xin Ye<sup>a,\*</sup>, Fang Zhu<sup>a</sup>, Xin Yang<sup>b</sup>, Gangfeng Ouyang<sup>a,c,d,\*\*</sup>

<sup>a</sup> MOE Key Laboratory of Bioinorganic and Synthetic Chemistry, School of Chemistry, Sun Yat-sen University, Guangzhou 510006, China

<sup>b</sup> School of Environmental Science and Engineering, Guangdong Provincial Key Laboratory of Environmental Pollution Control and Remediation Technology, Sun Yat-sen University, Guangzhou 510275, China

<sup>c</sup> Guangdong Provincial Key Laboratory of Chemical Measurement and Emergency Test Technology, Institute of Analysis, Guangdong Academy of Sciences (China National Analytical Center, Guangzhou), Guangzhou 510070, China

<sup>d</sup> Chemistry College, Center of Advanced Analysis and Gene Sequencing, Zhengzhou University, Zhengzhou 450001, China



### ARTICLE INFO

#### Keywords:

Conjugated polymer  
Electron donor-acceptor structure  
Photocatalytic degradation  
Hydrogen peroxide  
Excitonic separation

### ABSTRACT

The regulation of reactive oxygen species (ROS) in photocatalytic processes remains insufficiently explored. Herein, three triazine-based conjugated polymers were designed to regulate ROS by tuning structures. Strong superoxide radical was generated together with hydrogen peroxide through the electron transfer from the photocatalysts to oxygen, when electron donor-acceptor (D-A) structures were constructed in the photocatalysts. By sharp contrast, singlet O<sub>2</sub> that was generated via energy transfer was the dominant ROS on the photocatalyst with a symmetric structure. It was demonstrated that the separation of excitons in the D-A photocatalysts was much more efficient. By using the most efficient D-A photocatalyst, phenol was degraded completely within 60 min, and 1351 μmol·h<sup>-1</sup>·g<sup>-1</sup> of hydrogen peroxide was generated simultaneously. The photodegradation performance and the photosynthesis performance both ranked among the highest ones. The regulation of ROS by tuning the structures of photocatalysts opens new prospects for the design of efficient photocatalysts at the molecular level.

### 1. Introduction

The removal of organic pollutants has aroused wide attention in the scientific community [1–3]. Compared to the other methods for wastewater treatment, i.e. the Fenton method and the electrocatalytic method, the photocatalytic method is much preferred in terms of its low financial cost for wastewater treatment [4–6]. During photocatalysis, catalysts absorb sunlight to produce photo-induced charge carriers including electrons and holes that subsequently react with dissolved oxygen and water to generate reactive oxygen species (ROS), which can further degrade the organic pollutants in water [7]. Hence, sufficient photo-induced charge carriers are crucial for photocatalysis because they are the feedstocks to trigger the photochemical processes.

In recent years, conjugated polymeric photocatalysts have attracted numerous attentions owing to their tunable structures and properties [8]. Among them, g-C<sub>3</sub>N<sub>4</sub> was a typical representative [9]. Although vast

effective strategies have been reported to improve the photocatalytic efficiency of pristine g-C<sub>3</sub>N<sub>4</sub>, the inherent defects limited its further improvement, i.e. the high activation energy of exciton (E<sub>a</sub>) [10,11]. Therefore, it is of great significance to design and synthesize more efficient conjugated polymeric photocatalysts. Recently, owing to the development of synthetic methodologies, the geometries, functional groups, and linking sites of the aromatic building blocks are tunable to derive diverse conjugated polymers, offering great flexibility in the design of the skeletons and morphologies [12–16]. As a result, their physicochemical properties can be precisely tuned at the molecular level as well. However, the degradation of organic pollutants by most conjugated polymers is moderate [17–21], because their main reactive oxygen species (ROS) is singlet oxygen (<sup>1</sup>O<sub>2</sub>) with weak oxidation and short life, rather than superoxide radicals (·O<sub>2</sub><sup>·</sup>) with strong oxidation and longer life.

The production pathways of <sup>1</sup>O<sub>2</sub> and ·O<sub>2</sub><sup>·</sup> are substantially different

\* Corresponding author.

\*\* Corresponding author at: MOE Key Laboratory of Bioinorganic and Synthetic Chemistry, School of Chemistry, Sun Yat-sen University, Guangzhou 510006, China.

E-mail addresses: [yeuxin5@mail.sysu.edu.cn](mailto:yeuxin5@mail.sysu.edu.cn) (Y.-X. Ye), [cesoyg@mail.sysu.edu.cn](mailto:cesoyg@mail.sysu.edu.cn) (G. Ouyang).

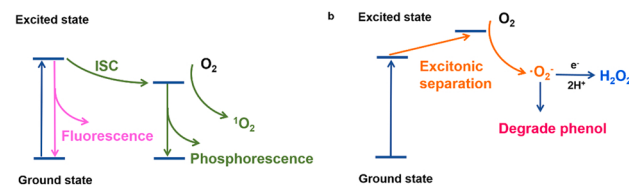


Fig. 1. The production pathways of (a)  $^1\text{O}_2$  and (b)  $\text{O}_2^-$ .

(Fig. 1).  $^1\text{O}_2$  is generated from energy transfer from the triplet excitons to  $\text{O}_2$ . On the other hand, the formation process of  $\text{O}_2^-$  is based on the electron transfer from free electrons after excitonic separation. Similarly, hydrogen peroxide ( $\text{H}_2\text{O}_2$ ) is also generated via electron transfer from free electrons. The free electrons reduce oxygen to generate  $\text{O}_2^-$  through single-electron reduction, or  $\text{H}_2\text{O}_2$  through two-electron reduction. It has been documented that the formation of triplet excitons and the formation of free electrons are two competing pathways. When the triplet excitons form from singlet excitons via intersystem crossing, they will produce phosphorescence in the argon atmosphere or react with  $\text{O}_2$  to generate  $^1\text{O}_2$ , and no longer separate into charge carriers [6,22]. Therefore, exciton activation energy ( $E_a$ ) that determines whether singlet excitons are inclined to separate is crucial for the generation of different ROS. In other words, the decrease of  $E_a$  would lead to the generation of more  $\text{O}_2^-$  rather than  $^1\text{O}_2$ .

One of the most efficient strategies for promoting the separation of excitons in organic photocatalysts is to construct electron donor-acceptor (D-A) structures through alternately connecting electron-rich and electron-deficiency units [7,23,24]. In a D-A photocatalyst, the separation of singlet excitons is promoted and the radiative recombination is suppressed. Through constructing the D-A system, the  $E_a$  can be decreased from more than 100 meV to dozens meV. Moreover, through improving the co-planarity between electron donor and acceptor, the  $E_a$  could be further reduced to nearly 40 meV [23]. However, it remains unexplored to control the types of ROS by tuning the structures of conjugated polymeric photocatalysts.

Herein, we present that the types of ROS could be rationally regulated by adjusting the number of aromatic rings in triazine-based conjugated polymers (TPT-CPs). More specifically, naphthyl and anthranyl groups were respectively introduced to the TPT-CPs to afford two D-A polymers termed as TPT-2 and TPT-3. Compared to the control TPT-CPs with a non-D-A structure (termed as TPT-1), TPT-2 and TPT-3 exhibited more efficient exciton separation. Moreover, attributed to the efficient separation of excitons into holes and electrons, the oxygen reduction products on TPT-2 and TPT-3 were superoxide radicals and  $\text{H}_2\text{O}_2$ , instead of singlet oxygen on TPT-1. It was recorded that the  $E_a$  of TPT-3 was much lower than that of TPT-1. Remarkably, TPT-3 achieved the highest efficiency in generating reactive oxygen species in open air, phenol was completely degraded in only 60 min, and  $1351 \mu\text{mol}\cdot\text{h}^{-1}\cdot\text{g}^{-1}$  of hydrogen peroxide was generated simultaneously. The AQY of TPT-3 reached as high as 18%, 15%, and 11% at 405, 425, and 450 nm respectively. In addition, the efficiency of solar-to-chemical conversion was 0.17% in pure water and open air, which was higher than the average solar-to-biomass conversion efficiency of typical plants ( $\sim 0.1\%$ ). This work represents remarkable progress in regulating ROS by tuning the structures of photocatalysts. Such a finding is inspiring for the design of efficient organic photocatalysts at the molecular level.

## 2. Experimental section

### 2.1. Materials

2,6-dibromoanthracene and 4,4'-(ethyne-1,2-diyl)dibenzonitrile were purchased from Shanghai Tensus Biotech Co., Ltd. 2,6-dibromo-naphthalene was obtained from Shanghai Meryer Chemical Technology Co., Ltd. 4-ethynylbenzonitrile and Trifluoromethanesulfonic acid

were purchased from Shanghai Energy Chemical Co., Ltd. Bis(triphenylphosphine)palladium(II)dichloride, Triethylamine and Tetrahydrofuran were purchased from Shanghai Macklin Biochemical Co., Ltd. Cuprous iodide was supplied by Shanghai Bide Pharmatech Ltd.

### 2.2. Characterization

Fourier transform infrared spectra (FT-IR) was performed on a PerkinElmer Frontier spectrometer. UV-visible spectroscopy (UV-Vis) was carried out on a Shimadzu UV-3600 spectrometer. The crystalline phases were characterized by a powder X-ray diffraction instrument (D-MAX 2200 VPC) at 40 kV and 26 mA. X-ray photoelectron spectroscopy (XPS) measurements were tested by using an ESCALab 250 spectrometer. Raman spectra were collected using a Laser Microscopic Confocal Raman Spectrometer (Renishaw inVia) at 365 nm. Photoluminescence (PL) spectra were conducted on an FLS 1000 spectrometer.  $\text{N}_2$  isotherms and surface area measurements were performed on a JW-BK200C instrument. SEM images were obtained using a SU8010 emission scanning electron microscope operated at 10 kV. TEM images were taken by using JEM-ARM200P.

### 2.3. The synthesis of TPT-CPs

#### Synthesis of TPT-1.

2 mL of trifluoromethanesulfonic acid was charged into a pre-dried flask under Ar atmosphere at 0 °C. 200 mg of 4,4'-(ethyne-1,2-diyl) dibenzonitrile in 10 mL of  $\text{CHCl}_3$  was added into the flask dropwise over 30 min and stirred for 2 h. Then the suspension was warmed up to 25 °C and stirred for another 2 h before left for 2 h at 100 °C. The obtained solid was quenched in cold water and washed with excess diluted ammonia,  $\text{CHCl}_3$  and water. After vacuum dried at 100 °C, the finally obtained solid was grounded into powder and subjected to ultrasonication for 36 h in water.

#### Synthesis of TPT-2.

3 mL of trifluoromethanesulfonic acid was charged into a pre-dried flask under Ar atmosphere at 0 °C. 200 mg of 4,4'-(naphthalene-2,6-diylbis(ethyne-2,1-diyl)) dibenzonitrile in 20 mL of  $\text{CHCl}_3$  was added into the flask dropwise over 30 min and stirred for 2 h. Then the suspension was warmed up to 25 °C and stirred for another 2 h before leaving overnight at 100 °C. The obtained solid was quenched in cold water and washed with excess diluted ammonia and water. After vacuum dried at 100 °C, the finally obtained solid was grounded into powder and subjected to ultrasonication for 36 h in water.

#### Synthesis of TPT-3.

TPT-3 was synthesized via the same procedure and the same conditions as TPT-2.

### 2.4 Photocatalytic phenol degradation and $\text{H}_2\text{O}_2$ evolution synchronously experiments.

The catalytic performance of TPT-CPs was investigated by photocatalytic degradation of 10 ppm phenol under visible light (300 W Xe lamp, 400 nm cut-off filter) at room temperature. The average light intensity was kept at  $100 \text{ mW}\cdot\text{cm}^{-2}$ . Typically, 5 mg of the photocatalyst was dispersed in 10 mL of water containing 10 ppm phenol. All photodegradation solutions were stirred without lights for 30 min to reach adsorption-desorption equilibrium between the substances and the surface of catalysts.

The concentration of the pollutant was measured by extracting the reaction solution with a syringe topped with a  $0.22 \mu\text{m}$  syringe filter every 30 min and monitored by a high-performance liquid chromatography (HPLC, Thermo Fisher Scientific Inc., USA) equipped with a C18 column ( $4.6 \times 250 \text{ mm}$ ,  $5 \mu\text{m}$ , Thermo Fisher).

Simultaneous monitoring of hydrogen peroxide generation during pollutant degradation. The concentration of  $\text{H}_2\text{O}_2$  was quantified by a TMB- $\text{H}_2\text{O}_2$ -HRP enzymatic assay.



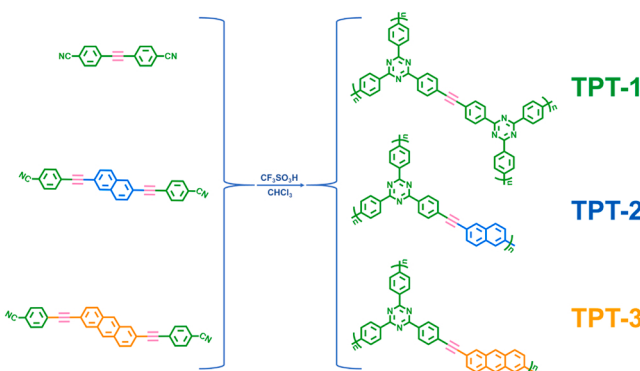


Fig. 2. Scheme of the synthesis of TPT-CPs.

To obtain the calibration curve, TMB and HRP were added to the  $\text{H}_2\text{O}_2$  solution with known concentrations. After 3 min, 10  $\mu\text{L}$  HCl was added and measured by the UV-vis spectroscopy at 450 nm. Based on the linear relationship between signal intensity and  $\text{H}_2\text{O}_2$  concentration, this standard calibration curve was used for quantifying the concentration of produced  $\text{H}_2\text{O}_2$ .

#### 2.4. Photoelectrochemical measurements

Electrochemical measurements were conducted on an electrochemical workstation (CHI 760E Instruments) in a three-electrode cell system. A Standard three-electrode setup was used with Pt-wire and Ag/AgCl (saturated KCl) as counter and reference electrodes. A 300 W Xe

lamp was used as the illumination source. As for polymer films, 5.0 mg photocatalyst was dispersed in ethanol and Nafion mixed solution (180  $\mu\text{L}$  + 20  $\mu\text{L}$ ). The mixture was dropped on top of a glassy carbon working electrode and  $1.5 \times 1 \text{ cm}^2$  FTO glass, and the solvent was evaporated under 60 °C for at least 30 min. The Mott-Schottky and photocurrent measurements used FTO electrode as the working electrode. The glassy carbon electrodes were used as the working electrode in Cyclic voltammograms and electrochemical impedance spectroscopy (EIS). The Mott-Schottky measurements were carried out in 0.5 M  $\text{Na}_2\text{SO}_4$  solution with different alternating current frequencies. The electrochemical impedance spectroscopy (EIS) and Cyclic voltammograms were performed in 0.1 M phosphate buffer solution (pH=7). The photocurrent measurements were measured in 0.1 M  $\text{Na}_2\text{SO}_4$  solution.

#### 2.5. Density functional theory (DFT) calculation

The DFT calculation were performed as implemented in Gaussian 09 D.01 program package [25]. Grimme-D3 was used for dispersion correction [26]. GaussView6 was applied to visualization [27]. The geometry optimizations were performed using PBE0/6-31 G(g,d) level of theory [28].

### 3. Results and discussion

#### 3.1. The synthesis and characterization of TPT-CPs

Three TPT-CPs were synthesized from their corresponding nitrile precursors via trimerization reactions catalyzed by trifluoromethanesulfonic acid as illustrated in Fig. 2 [29–31]. Fourier

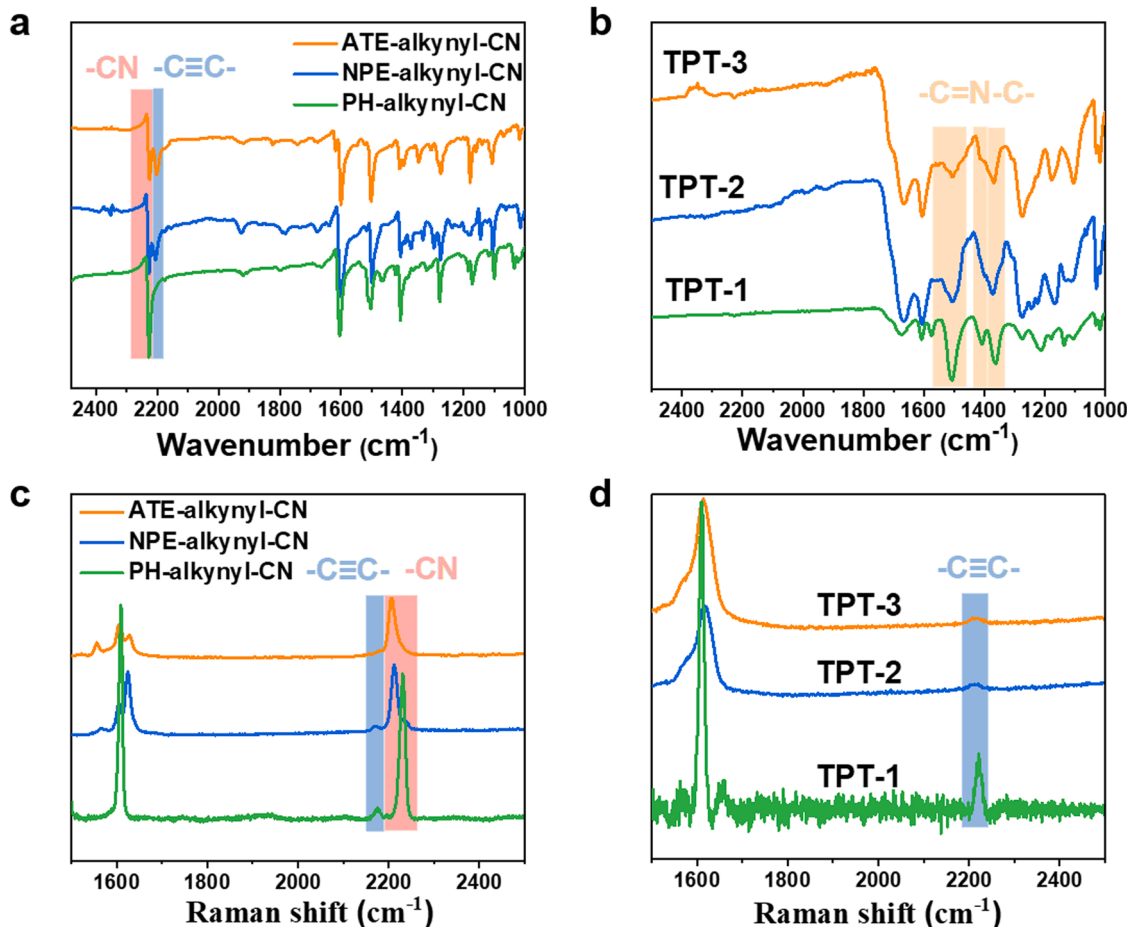


Fig. 3. FT-IR spectra of (a) nitrile precursors and (b) TPT-CPs. Raman spectra of (c) nitrile precursors and (d) TPT-CPs.

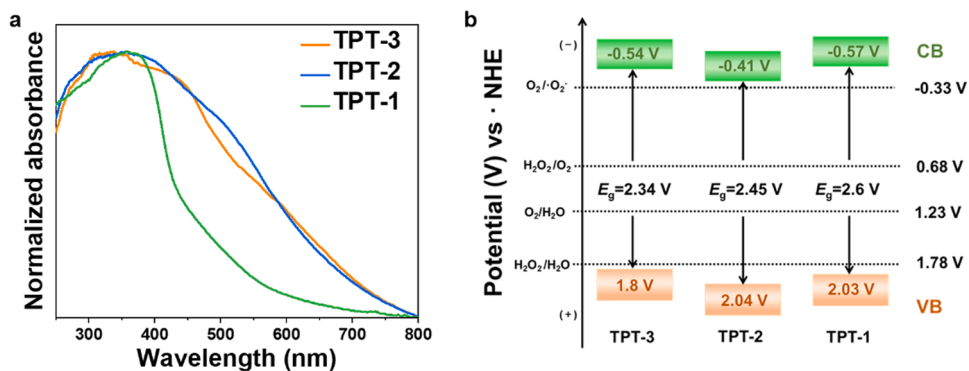


Fig. 4. (a) The UV-Visible diffuse reflectance spectra of TPT-CPs. (b) The electronic band structure of TPT-CPs.

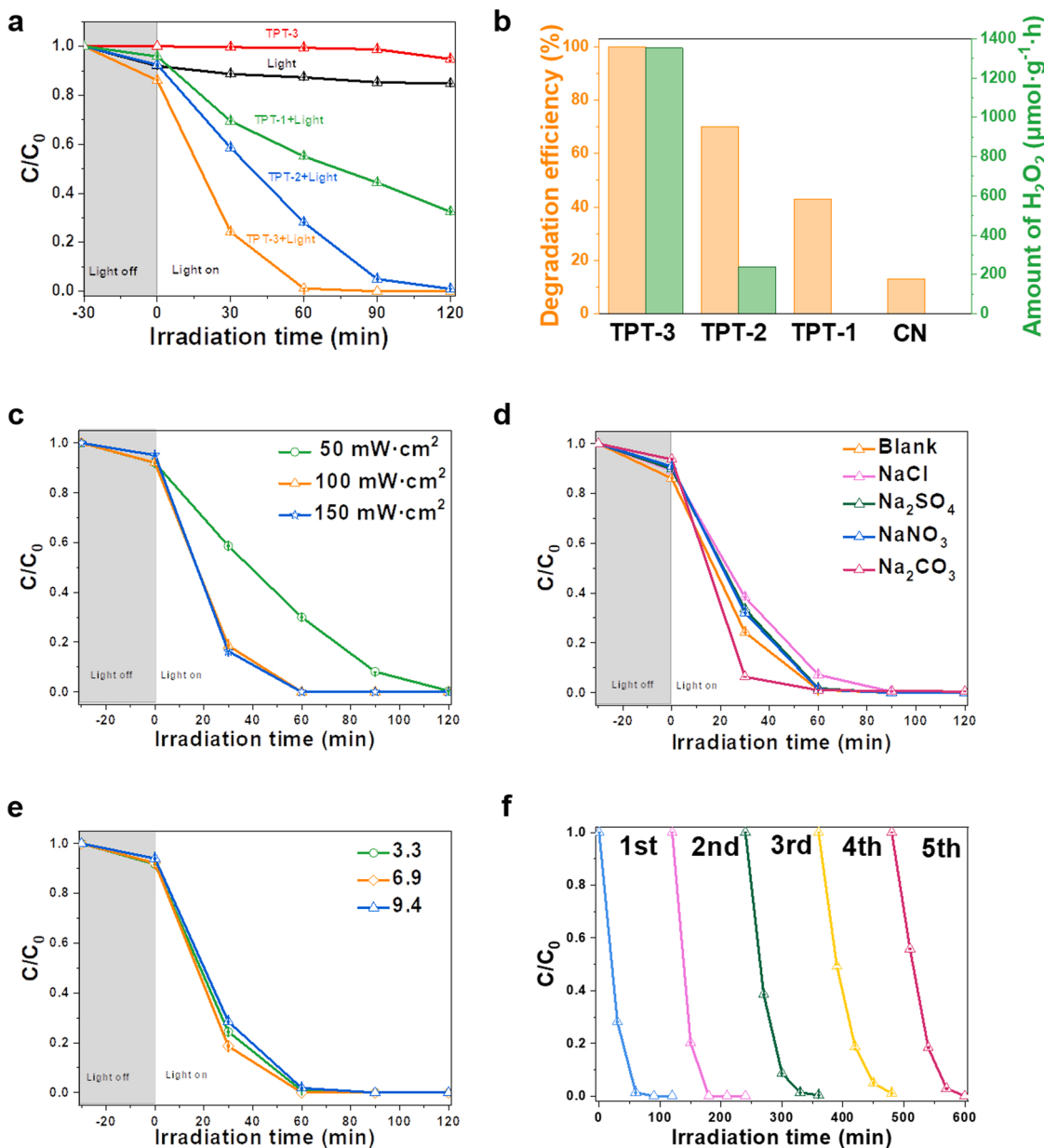


Fig. 5. (a) Phenol degradation time profiles of TPT-CPs. (b) The generation of  $H_2O_2$  and degradation efficiency of phenol for TPT-CPs and CN. Phenol degradation time profiles of TPT-3 (c) in different light intensity, (d) in different anions and (e) in different pH. (f) Cycling phenol degradation test of TPT-3.

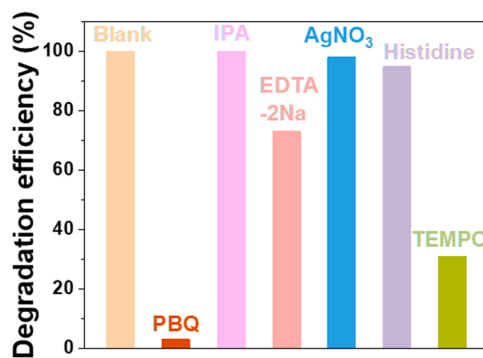


Fig. 6. Phenol degradation efficiency upon the addition of different sacrificial agents.

transformed infrared (FTIR) spectra were first used to characterize the structures of the nitrile precursors and corresponding TPT-CPs. As shown in Fig. 3a, all nitrile precursors exhibit an evident peak at  $2229\text{ cm}^{-1}$  that was attributed to the stretching of the carbon-nitrogen triple bond in the terminal cyano groups [32]. This peak disappeared after trimerization, and three strong peaks at 1504, 1406, and  $1361\text{ cm}^{-1}$  appeared in the corresponding TPT-CPs (Fig. 3b), which were assigned to the stretching and breathing modes of aromatic carbon-nitrogen bonds in the 1,3,5-triazine conjugated structure [33, 34]. Besides, Raman spectroscopy was also used to confirm these results (Fig. 3c). All nitrile precursors exhibit an obvious peak at  $2206\text{--}2232\text{ cm}^{-1}$  that was attributed to the cyano groups [35]. After the trimerization reaction, the electron-withdrawing effect of the cyano group disappears and the corresponding Raman peak appears in a higher

position due to the increased effective force constants (Fig. 3d) [21]. On the other hand, the peak at  $2215\text{ cm}^{-1}$  which was assigned to the alkynyl moieties was reserved in Raman spectra, indicating the alkynyl moieties of all the TPT-CPs were maintained [29]. Moreover, the peaks at around  $399.3\text{ eV}$  deconvoluted from the N 1 s peak in X-ray photoelectron spectroscopy (XPS) spectra of all TPT-CPs also confirmed the formation of the triazine structure (Fig. S1) [36]. All of these spectroscopic characterizations unambiguously validated the formation of the desired triazine frameworks via trimerization reactions.

The powder X-ray diffraction (PXRD) spectra of all the TPT-CPs showed no obvious sharp peak, which demonstrated the structure of amorphous carbon present in the polymers (Fig. S2) [37]. The broad peaks at around 20 degrees indicated that all TPT-CPs were laminar stacking structures based on strong  $\pi\text{-}\pi$  action. The amorphous laminar stacking structure in TPT-CPs were also confirmed by scanning electron microscopy (SEM) images and transmission electron microscopy (TEM) images (Figs. S3 and S4). The measured BET (Brunauer-Emmett-Teller) surface areas of TPT-1, TPT-2, and TPT-3 were  $37.594$ ,  $14.164$ , and  $16.025\text{ m}^2\cdot\text{g}^{-1}$ , respectively (Fig. S5). And the average pore sizes of TPT-1, TPT-2, and TPT-3 were  $1.766$ ,  $2.769$ , and  $2.769\text{ nm}$ , respectively. Both the BET surface areas and pore sizes of TPT-CPs were consistent with the previous studies [29,31].

### 3.2 Electronic structures of TPT-CPs.

As shown in Fig. 4a, TPT-2 and TPT-3 exhibited much broader absorption in visible regions than TPT-1. This proved that D-A based photocatalysts were beneficial to widen the light absorption range of the visible light regions. According to the Mott-Schottky test, the Flat-band potential of TPT-1, TPT-2, and TPT-3 were fitting to be  $-0.27$ ,  $-0.11$ , and  $-0.24\text{ eV}$  versus RHE, respectively (Figure S6). Also, the TPT-CPs were n-type semiconductors because the slopes of the tangents of the TPT-CPs were positive. For n-type semiconductors, the flat-band

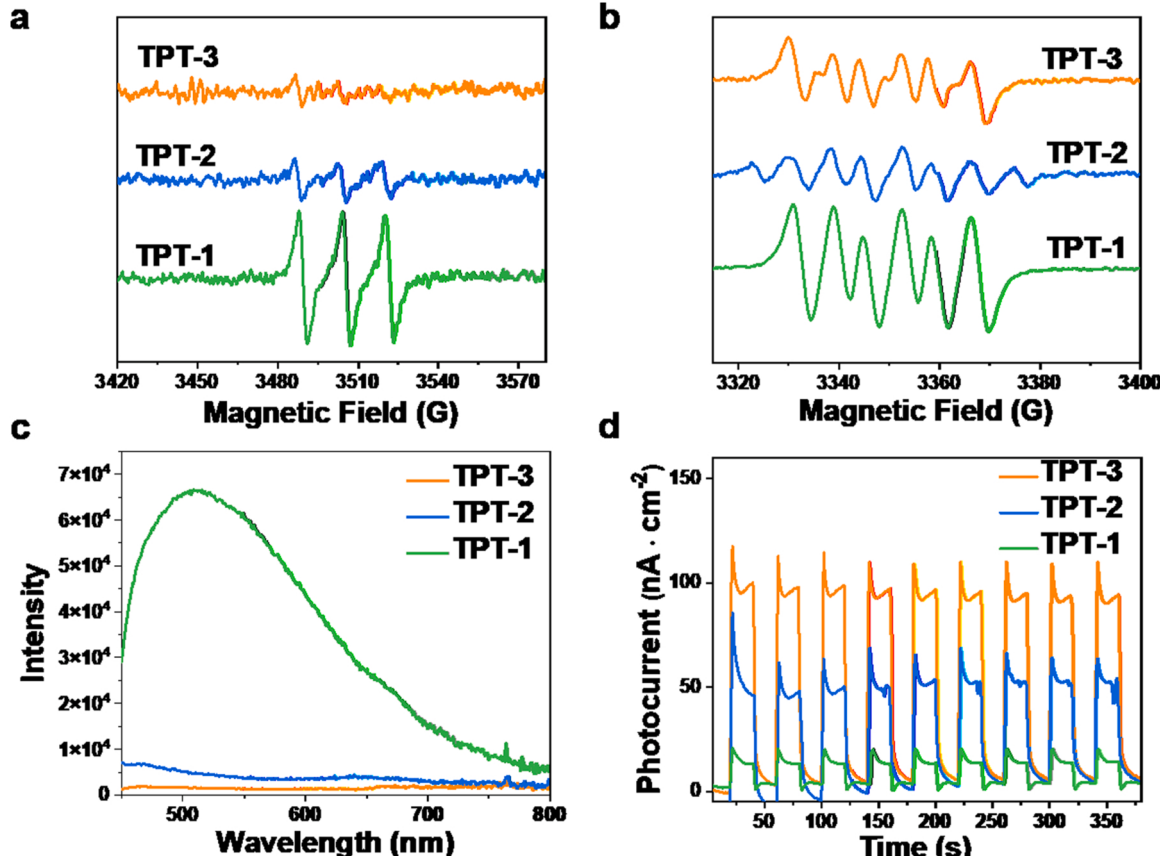
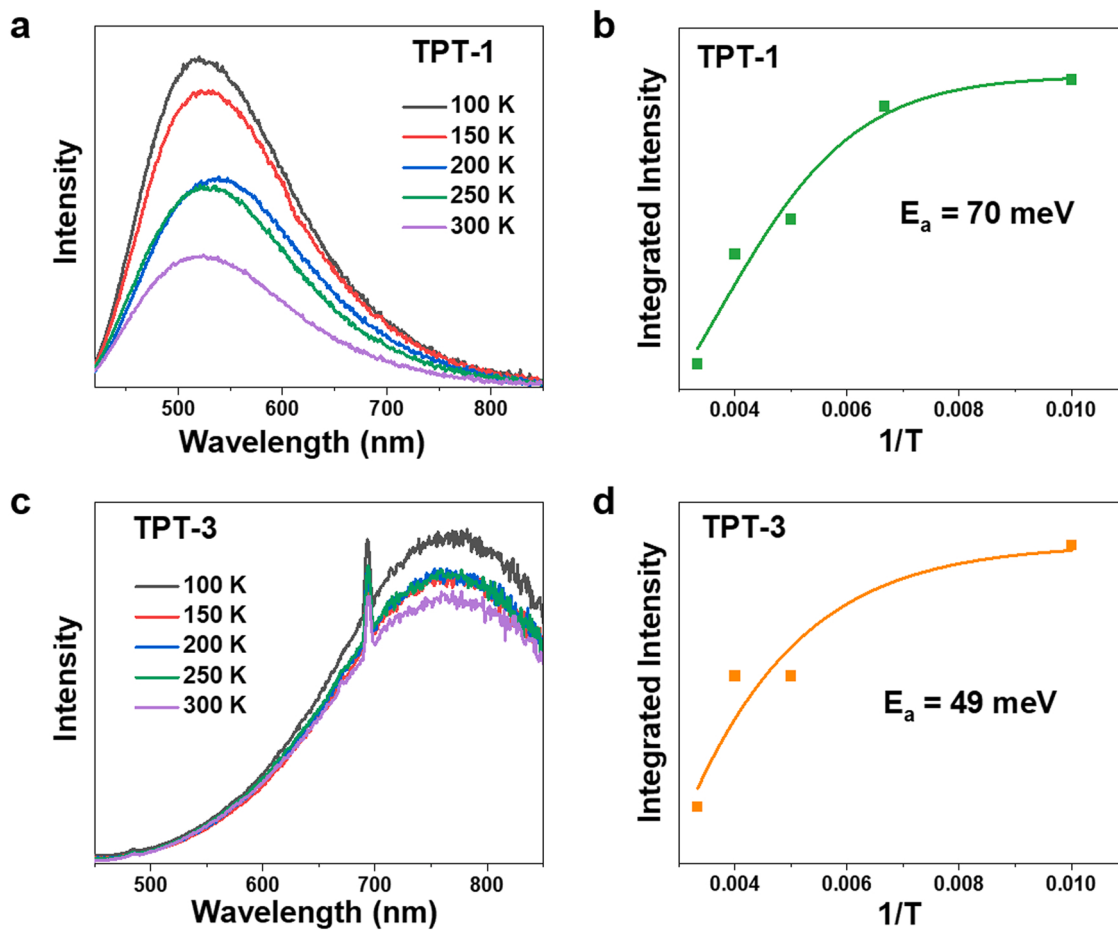


Fig. 7. ESR spectra of TPT-CPs in the presence of (a) TEMP and (b) DMPO in  $\text{O}_2$  atmosphere under visible light irradiation. (c) Photoluminescence spectra of TPT-CPs. (d) Current-Time (I-t) curves of TPT-CPs under visible light illumination.



**Fig. 8.** Temperature-dependent photoluminescence (PL) spectra for (a) TPT-1 and (c) TPT-3. Evolution of PL intensity as a function of temperature from 100 to 300 K for (b) TPT-1 and (d) TPT-3.

potential is 0.1–0.3 V more positive than the conduction band potential. The positions of conduction band minima (CBM) of TPT-1, TPT-2, and TPT-3 were fitting to be  $-0.57$ ,  $-0.41$ , and  $-0.54$  eV versus RHE, respectively. Cyclic voltammograms (CV) were recorded to explore the highest occupied molecular orbital (HOMO) (Fig. S7). The HOMO energy levels are calculated according to the oxidation onset potentials. The HOMO energy levels of TPT-1, TPT-2, and TPT-3 were located at 2.03, 2.04, and 1.8 eV versus RHE, respectively. The valence band maxima (VBM) consisted of the highest occupied molecular orbital (HOMO). By using the equation of  $E_g = E_{VBM} - E_{CBM}$ , their corresponding band gap energies ( $E_g$ ) were calculated to be 2.6, 2.45, and 2.34 eV versus RHE. Hence, the electronic band structures of TPT-CPs were illustrated in Fig. 4b. As shown in Fig. 4b, when the conjugate properties of the electron donor were increased, the overall oxidation capacity of the photocatalyst was weakened, and the reducing capacity was enhanced. Moreover, all of the TPT-CPs were potential to reduce  $O_2$  to  $O_2^-$  via single-electron transfer.

### 3.2. Photocatalytic performances of TPT-CPs

The photocatalytic activities of TPT-CPs were evaluated via the degradation of phenol and the generation of  $H_2O_2$  simultaneously. The photocatalytic experiment was conducted under the irradiation of simulated sunlight ( $\lambda > 400 \text{ nm}$ ,  $100 \text{ mW} \cdot \text{cm}^{-2}$ ) and in open air. No additional organic reagent was added to the reaction vials. The degradation time profiles were presented in Fig. 5a, where  $C$  and  $C_0$  corresponded to the instant and the initial concentrations of the phenol aqueous solution, respectively. In the darkness, all TPT-CPs showed negligible adsorption capacities to phenol. Under visible light

( $100 \text{ mW} \cdot \text{cm}^{-2}$ ), the phenol degradation rate by TPT-3 was the highest. Phenol was degraded to an undetectable level within 60 min. Simultaneously, as high as  $1351 \mu\text{mol} \cdot \text{g}^{-1}$  of  $H_2O_2$  was generated (Fig. 5b).  $H_2O_2$  was a green oxidant for the potential application in photocatalysis-self-Fenton reaction for deeper degradation of phenol [38,39]. Notably, both the photosynthetic rate of  $H_2O_2$  and the degradation rate of phenol on TPT-3 are among the highest in the reported works, even compared to other single functional system, i.e. photosynthetic systems or sole photodegradation systems (Tables S1 and S2). By contrast, TPT-1 and TPT-2 degraded only 43% and 70% of phenol in the same 60 min with undetectable and only  $238 \mu\text{mol} \cdot \text{g}^{-1}$  of  $H_2O_2$  was produced, respectively (Figs. 5a and 5b). Notably, the efficiencies of both D-A-based TPT-2 and TPT-3 were much higher than the non-D-A-based TPT-1. For comparison, using the most studied conjugated polymer  $g\text{-C}_3\text{N}_4$  as the photocatalyst, 13% of phenol was degraded, and undetectable  $H_2O_2$  was generated (Fig. 5b). TPT-3 degraded phenol completely within 2 h even though the concentration of phenol was up to 30 ppm (Figure. S8). Moreover, TPT-3 degraded phenol completely within 2 h even though the light intensity was reduced to  $50 \text{ mW} \cdot \text{cm}^{-2}$  (Fig. 5c). The excellent photocatalytic activity of TPT-3 indicated the electron donor had a significant impact on photocatalytic efficiency. This highlighted that D-A-based conjugated polymer is a promising photocatalytic material for organic pollutant degradation.

In addition to the outstanding efficiency, the anti-interference capability is also an important factor to evaluate the performance of photocatalysts. As shown in Fig. 5d, TPT-3 exhibited excellent resistance to anionic interferences. The anions that were regularly present in water, i.e.  $Cl^-$ ,  $SO_4^{2-}$ ,  $NO_3^-$ ,  $CO_3^{2-}$ , showed little effect on the phenol degradation efficiency of TPT-3. Moreover, TPT-3 maintained the activity over a

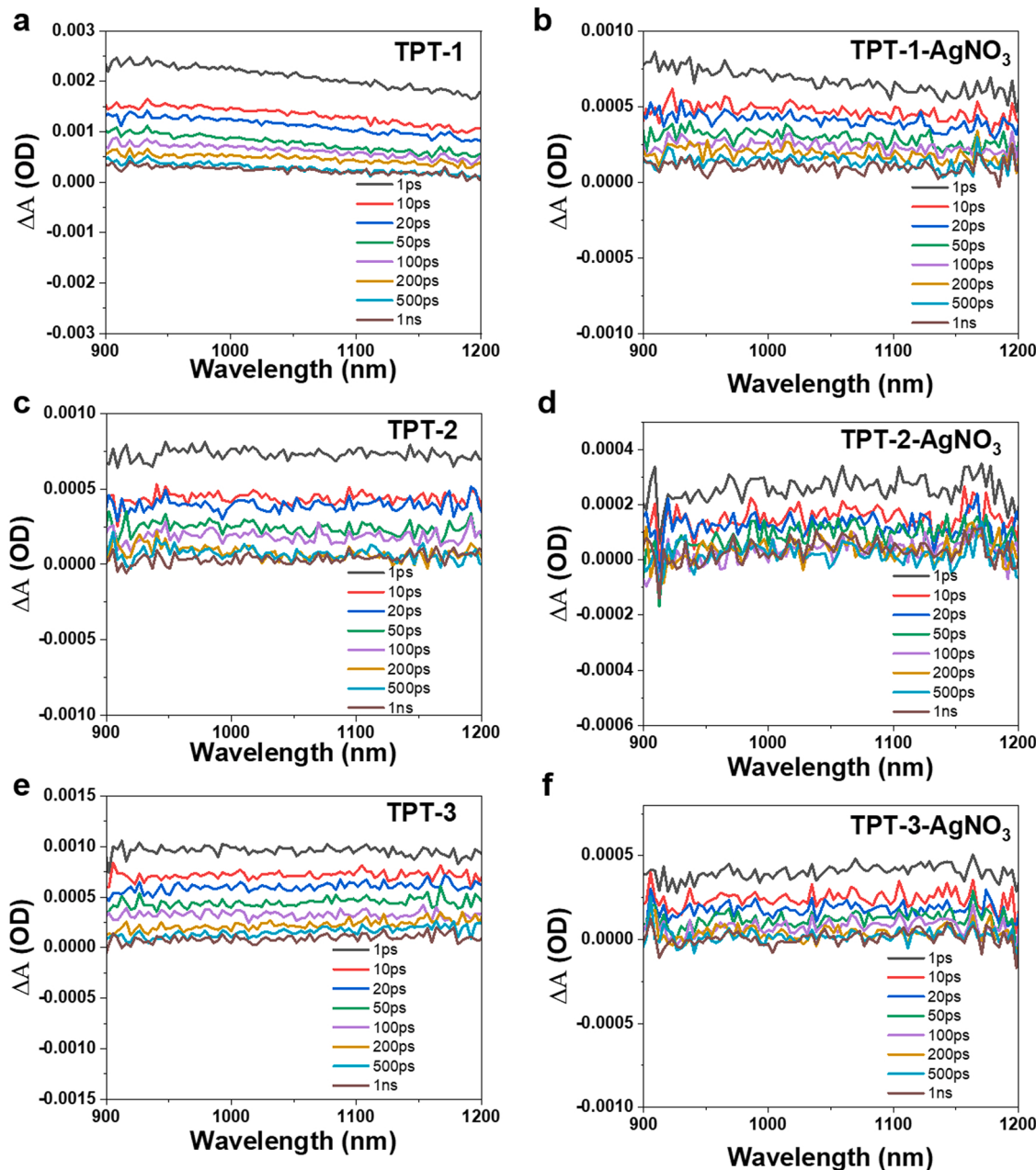


**Fig. 9.** TA spectra of TPT-CPs with or without  $\text{AgNO}_3$  (10 mM). (a) TPT-1, (b) TPT-1 with  $\text{AgNO}_3$ , (c) TPT-2, (d) TPT-2 with  $\text{AgNO}_3$ , (e) TPT-3, (f) TPT-3 with  $\text{AgNO}_3$ .

wide pH range from 3 to 9 (Fig. 5e).

The recyclability of TPT-3 was assessed by repeated phenol degradation experiments over the same catalyst. Five consecutive degradation cycles using TPT-3 were shown in Fig. 5f, and the phenol degradation efficiency could be maintained for at least five cycles. The FTIR spectra, Raman spectra, XRD, SEM, and TEM images of TPT-3 were recorded after five consecutive photocatalytic reactions, and no apparent change was observed (Fig. S9). These results indicated that TPT-3 showed excellent recyclability and stability.

### 3.3. The mechanism behind the excellent performance of TPT-3

To explore the photocatalytic mechanism of TPT-3 in the degradation of phenol, the related oxidative species in phenol degradation were characterized by radical trapping scavengers (Fig. 6). p-Benzoquinone (p-BQ), isopropyl alcohol (IPA), EDTA disodium (EDTA-2Na), silver nitrate ( $\text{AgNO}_3$ ), and histidine were used to scavenge superoxide radical

( $\cdot\text{O}_2^-$ ), hydroxyl radical ( $\cdot\text{OH}$ ), hole ( $\text{h}^+$ ), electron ( $\text{e}^-$ ) and singlet oxygen ( ${}^1\text{O}_2$ ), respectively [6]. In the presence of p-BQ and EDTA-2Na, the degradation of phenol was significantly inhibited, which indicated that  $\text{O}_2$  and  $\text{h}^+$  were the main oxidative species in the photocatalytic degradation of phenol. To further confirm this result, TEMPO, another  $\cdot\text{O}_2$  scavenger was also used (Fig. 6) [40]. Similarly, the phenol degradation was also obviously inhibited. Thus, the main reactive oxygen species (ROS) in phenol degradation was generated through the electron-transfer process from TPT-3 to oxygen instead of the energy-transfer process that would produce  ${}^1\text{O}_2$ .

For further investigation of the ROS generated in the photocatalytic process, the ESR measurement was used to characterize the ROS generated in TPT-CPs. As shown in Fig. 7a and 7b, only TPT-1 exhibited the typical signal of  ${}^1\text{O}_2$ , and all the TPT-CPs displayed the typical signal of  $\cdot\text{O}_2^-$ . In addition, the amount of triplet exciton was characterized through phosphorescence spectroscopy under an argon atmosphere (Fig. S10) [41]. Remarkably, TPT-2 and TPT-3 exhibited much lower

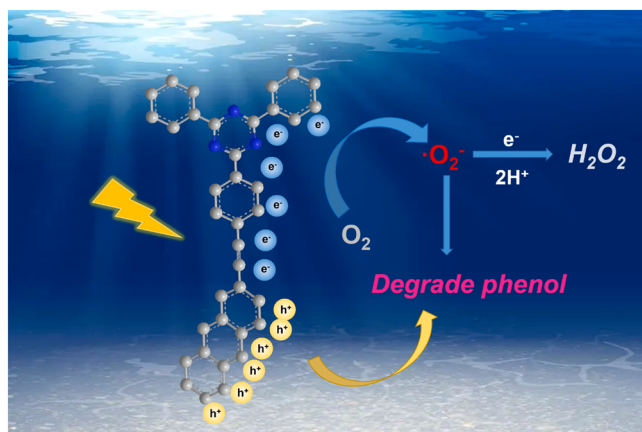


**Fig. 10.** A possible mechanism for photocatalytic degradation of phenol and generation of  $\text{H}_2\text{O}_2$  over TPT-3.

phosphorescence emission than that TPT-1. This demonstrated the excitons in these D-A-based TPT-CPs preferred to separate into photo-induced carriers rather than recombine to generate phosphoresce.

Furthermore, to reveal the mechanism of photo-induced carrier generation, steady-state fluorescence (FL) spectroscopy was used to characterize the radiative recombination of excitons. The intensity of TPT-CPs was in the order of TPT-3 < TPT-2 < TPT-1, where the FL intensity of TPT-2 and TPT-3 was much weaker compared to that of TPT-1 (Fig. 7c). Further, the FL quantum yields of TPT-2 and TPT-3 were 0.01% and undetectable, respectively, which were much lower than that of TPT-1 (0.11%). This demonstrated that radiative recombination was greatly suppressed through the construction of the D-A structure [23]. Temperature-dependent PL spectra of the TPT-CPs were recorded to further investigate the mechanism behind the efficient separation of excitons (Fig. 8 and Fig. S11) [23,24]. A thermal quenching phenomenon of PL emission in the temperature range from 100 to 300 K was observed for the TPT-CPs. By fitting the integrated PL intensities as a function of temperature using the Arrhenius equation,  $I(T) = I_0/[1 + A\exp(-E_a/k_B T)]$ , the  $E_a$  of the PL quenching process was estimated to be 70, 64, and 46 meV, for TPT-1, TPT-2 and TPT-3 respectively. The much lower  $E_a$  of TPT-3 demonstrated that the separation of its excitons occurred more readily than that in TPT-1 and TPT-2, which was consistent with the aforementioned room-temperature PL intensities. Thus, it can be surmised that the construction of a D-A-based structure is advantageous for promoting exciton separation in TPT-CPs photocatalysts by reducing the  $E_a$ . In the transient photocurrent experiment, the photocurrent intensity of TPT-3 was significantly higher than that of TPT-2, and the photocurrent intensity of TPT-1 was the lowest (Fig. 7d), demonstrating D-A-based photocatalyst generated more photo-generated carriers due to low exciton binding energy ( $E_a$ ).

Moreover, density functional theory (DFT) calculations were conducted for TPT-CPs to further investigate the intrinsic mechanism behind the reduced  $E_a$  in TPT-CPs. As shown in Fig. S12, both the LUMO and HOMO in TPT-1 were evenly distributed throughout the unit and almost exactly overlapped with each other. The overlap between the HOMO and LUMO in TPT-1 caused radiative recombination of the exciton. On the contrary, in TPT-2 and TPT-3, the LUMO were mainly located in the TPT moieties, while the HOMO were mainly located in the naphthalene and anthracene moieties. By contrast, the separated distribution of the HOMO and LUMO promoted the separation of exciton in TPT-2 and TPT-3 [7]. The higher exciton separation efficiencies were also supported by the molecular dipoles. The dipoles of TPT-1, TPT-2, and TPT-3 were 0.0003, 0.9057, and 1.1287 D, respectively. This demonstrated the D-A based structure promoted the delocalization of electron cloud to reduce  $E_a$ , hence facilitating the separation of excitons in TPT-CPs.

The charge transfer process is another important parameter affecting photocatalytic activity. The charge transfer was further verified by electrochemical impedance spectroscopy (EIS), where TPT-2 and TPT-3 exhibited a smaller impedance semicircle radius, corresponding to their smaller charge transfer resistance (Fig. S13). This demonstrated the large molecular dipoles in the D-A based structure promoted charge transfer. Femtosecond transient absorption (TA) spectroscopy is a useful technique for studying ultrafast charge transfer. As shown in Fig. 9, photoexcitation of TPT-CPs yielded a broad absorption spanning from 900 to 1200 nm. In order to assign this broad peak, we measured the TA spectra of TPT-CPs with and without  $\text{AgNO}_3$  (Figure. S14). The amplitude decreased in the presence of  $\text{AgNO}_3$  as electron scavengers. Therefore, the signals observed at 900–1200 nm were assigned to photo-induced electrons. The lifetimes of photo-induced electrons were TPT-1 > TPT-2 > TPT-3, demonstrating the lifetime of photo-induced became shorter while the molecular dipole increased.

Based on the above results, we proposed a mechanism for photocatalytic degradation of phenol and generation of  $\text{H}_2\text{O}_2$  over TPT-3 in Fig. 10. Firstly, TPT-3 was excited to generate exciton under irradiation. Owing to the low  $E_a$  caused by the electron delocalization in its D-A structure, the exciton tended to separate into photo-induced electrons and holes instead of recombination to fluoresce or intersystem crossing to phosphoresce. The intramolecular transfer of photo-induced electrons from anthracene units to triazine units was facilitated through the D-A structure polarization effect. Then, the electrons at LUMO orbitals (including triazine and alkynyl units) reacted with the absorbed  $\text{O}_2$  to generate  $\cdot\text{O}_2$  or  $\text{H}_2\text{O}_2$  via one-electron and two-electron reduction processes, respectively. Meanwhile, the hole located in anthracene was also generated. Finally, in the presence of strong oxidizing  $\cdot\text{O}_2$  and holes, phenol in the water was effectively degraded, and a large amount of another ROS, i.e.  $\text{H}_2\text{O}_2$ , was remained for further potential applications, such as Fenton reactions.

#### 4. Conclusion

In summary, we report a highly efficient D-A-based dual-function photocatalyst. The target photocatalyst (TPT-3) exhibited outstanding photocatalytic efficiency, phenol was completely degraded in 60 min, and  $1351 \text{ umol}\cdot\text{h}^{-1}\cdot\text{g}^{-1}$  of hydrogen peroxide was generated simultaneously. The outstanding efficiency of this photocatalyst was owing to the introduction of a large electron donor into the TPT-CPs to construct the D-A-based structure, which highly promoted the generation and separation of excitons by the electron delocalization in D-A structure. The  $E_a$  was 46 meV for TPT-3, which was much lower than the non-D-A structure, i.e. 70 meV for TPT-1. The sufficient charge carriers in TPT-3 were verified by the large photocurrent and suppressed fluorescence and phosphorescence. Strong oxidative  $\cdot\text{O}_2$  and holes for phenol degradation were generated together with  $\text{H}_2\text{O}_2$ . This work establishes an efficient strategy to improve photocatalytic efficiency in conjugated polymeric photocatalysts via decreasing regulation of the formation of ROS.

#### CRediT authorship contribution statement

**Huijie Yan:** Data curation, Conceptualization, Methodology. **Yan-chun Deng:** Data curation, Methodology. **Minhui Shen:** Methodology. **Yu-Xin Ye:** Conceptualization, Supervision, Funding acquisition, Writing – review & editing. **Fang Zhu:** Funding acquisition. **Gangfeng Ouyang:** Project administration, Funding acquisition, Writing – review & editing.

#### Declaration of Competing Interest

The authors declare no conflicts of interest.

## Acknowledgments

We are grateful for the phosphorescence spectrometric determination supported by Ms. Yu-Xin Chen from the Instrumental Analysis and Research Center in Sun Yat-sen University. This work was supported by the National Natural Science Foundation of China (22036003, 22076222, and 21737006), Guangdong Provincial Key Research and Development Programme (2020B1111350002), the Natural Science Foundation of Guangdong Province (2020A1515011442), and the China Postdoctoral Science Foundation (2021M703677).

## Appendix A. Supporting information

Supplementary data associated with this article can be found in the online version at [doi:10.1016/j.apcatb.2022.121488](https://doi.org/10.1016/j.apcatb.2022.121488).

## References

- [1] M.A. Shannon, P.W. Bohn, M. Elimelech, J.G. Georgiadis, B.J. Mariñas, A. M. Mayes, Science and technology for water purification in the coming decades, *Nature* 452 (2008) 301–310.
- [2] S. Gupta Sayam, M. Stadler, A. Noser Christopher, A. Ghosh, B. Steinhoff, D. Lenoir, P. Horwitz Colin, K.-W. Schramm, J. Collins Terrence, Rapid total destruction of chlorophenols by activated hydrogen peroxide, *Science* 296 (2002) 326–328.
- [3] X. Li, X. Huang, S. Xi, S. Miao, J. Ding, W. Cai, S. Liu, X. Yang, H. Yang, J. Gao, J. Wang, Y. Huang, T. Zhang, B. Liu, Single cobalt atoms anchored on porous N-doped graphene with dual reaction sites for efficient fenton-like catalysis, *J. Am. Chem. Soc.* 140 (2018) 12469–12475.
- [4] Y. Mao, P. Wang, L. Li, Z. Chen, H. Wang, Y. Li, S. Zhan, Unravelling the synergy between oxygen vacancies and oxygen substitution in  $\text{BiO}_2-\text{x}$  for efficient molecular-oxygen activation, *Angew. Chem. Int. Ed.* 59 (2020) 3685–3690.
- [5] L. Su, P. Wang, X. Ma, J. Wang, S. Zhan, Regulating local electron density of iron single sites by introducing nitrogen vacancies for efficient photo-fenton process, *Angew. Chem. Int. Ed.* 60 (2021) 21261–21266.
- [6] D. Zhang, P. Wang, J. Wang, Y. Li, Y. Xia, S. Zhan, Tailoring of electronic and surface structures boosts exciton-triggering photocatalysis for singlet oxygen generation, *Proc. Natl. Acad. Sci. USA* 118 (2021), e2114729118.
- [7] J. Han, Z. Zhu, N. Li, D. Chen, Q. Xu, H. Li, J. He, J. Lu, Metalloporphyrin-based D-A type conjugated organic polymer nanotube for efficient photocatalytic degradation, *Appl. Catal. B* 291 (2021), 120108.
- [8] H. Bronstein, C.B. Nielsen, B.C. Schroeder, I. McCulloch, The role of chemical design in the performance of organic semiconductors, *Nat. Rev. Chem.* 4 (2020) 66–77.
- [9] X. Wang, K. Maeda, A. Thomas, K. Takanabe, G. Xin, J.M. Carlsson, K. Domen, M. Antonietti, A metal-free polymeric photocatalyst for hydrogen production from water under visible light, *Nat. Mater.* 8 (2009) 76–80.
- [10] V.S. Vyas, V.W.-h Lau, B.V. Lotsch, Soft photocatalysis: organic polymers for solar fuel production, *Chem. Mater.* 28 (2016) 5191–5204.
- [11] K. Schwinghammer, B. Tuffy, M.B. Mesch, E. Wirthner, C. Martineau, F. Taulelle, W. Schnick, J. Senker, B.V. Lotsch, Triazine-based carbon nitrides for visible-light-driven hydrogen, *Evol., Angew. Chem. Int. Ed.* 52 (2013) 2435–2439.
- [12] C. Zhao, Z. Chen, R. Shi, X. Yang, T. Zhang, Recent advances in conjugated polymers for visible-light-driven water splitting, *Adv. Mater.* 32 (2020) 1907296.
- [13] C. Dai, Y. Pan, B. Liu, Conjugated polymer nanomaterials for solar water splitting, *Adv. Energy Mater.* 10 (2020) 2002474.
- [14] Y. Wang, A. Vogel, M. Sachs, R.S. Sprick, L. Wilbraham, S.J.A. Moniz, R. Godin, M. A. Zwijnenburg, J.R. Durrant, A.I. Cooper, J. Tang, Current understanding and challenges of solar-driven hydrogen generation using polymeric photocatalysts, *Nat. Energy* 4 (2019) 746–760.
- [15] J. Byun, K.A.I. Zhang, Designing conjugated porous polymers for visible light-driven photocatalytic chemical transformations, *Mater. Horiz.* 7 (2020) 15–31.
- [16] G. Zhang, Z.-A. Lan, X. Wang, Conjugated polymers: catalysts for photocatalytic hydrogen, *Evol., Angew. Chem. Int. Ed.* 55 (2016) 15712–15727.
- [17] G. Lin, H. Ding, R. Chen, Z. Peng, B. Wang, C. Wang, 3D porphyrin-based covalent organic frameworks, *J. Am. Chem. Soc.* 139 (2017) 8705–8709.
- [18] L. Ma, Y. Liu, Y. Liu, S. Jiang, P. Li, Y. Hao, P. Shao, A. Yin, X. Feng, B. Wang, Ferrocene-linkage-facilitated charge separation in conjugated microporous, *Polym.*, *Angew. Chem. Int. Ed.* 58 (2019) 4221–4226.
- [19] J. Shen, R. Steinbach, J.M. Tobin, M. Mouro Nakata, M. Bower, M.R.S. McCoustra, H. Bridle, V. Arrighi, F. Vilela, Photoactive and metal-free polyamide-based polymers for water and wastewater treatment under visible light irradiation, *Appl. Catal. B* 193 (2016) 226–233.
- [20] X. Yang, F. Qian, G. Zou, M. Li, J. Lu, Y. Li, M. Bao, Facile fabrication of acidified  $\text{g-C}_3\text{N}_4/\text{g-C}_3\text{N}_4$  hybrids with enhanced photocatalysis performance under visible light irradiation, *Appl. Catal. B* 193 (2016) 22–35.
- [21] Y. Chen, J.-Q. Ren, X.-G. Zhang, D.-Y. Wu, A.-G. Shen, J.-M. Hu, Alkyne-modulated surface-enhanced raman scattering-palette for optical interference-free and multiplex cellular imaging, *Anal. Chem.* 88 (2016) 6115–6119.
- [22] A.J. Gillett, A. Privitera, R. Dilmurat, A. Karki, D. Qian, A. Pershin, G. Londi, W. K. Myers, J. Lee, J. Yuan, S.-J. Ko, M.K. Riede, F. Gao, G.C. Bazan, A. Rao, T.-Q. Nguyen, D. Beljonne, R.H. Friend, The role of charge recombination to triplet excitons in organic solar cells, *Nature* 597 (2021) 666–671.
- [23] Z.-A. Lan, M. Wu, Z. Fang, X. Chi, X. Chen, Y. Zhang, X. Wang, A. Fully, Coplanar donor–acceptor polymeric semiconductor with promoted charge separation kinetics for photochemistry, *Angew. Chem. Int. Ed.* 60 (2021) 16355–16359.
- [24] Z.-A. Lan, G. Zhang, X. Chen, Y. Zhang, K.A.I. Zhang, X. Wang, Reducing the Exciton Binding Energy of Donor–Acceptor-Based Conjugated Polymers to Promote Charge-Induced Reactions, *Angew. Chem. Int. Ed.* 58 (2019) 10236–10240.
- [25] M.J. Frisch, et al., Gaussian 09, Gaussian Inc, Wallingford CT, 2009.
- [26] S. Grimme, J. Antony, S. Ehrlich, H. Krieg, A consistent and accurate ab initio parametrization of density functional dispersion correction (DFT-D) for the 94 elements H–Pu, *J. Chem. Phys.* 132 (2010), 154104.
- [27] Roy Dennington et al., GaussView (Version 6.1.1, 2019).
- [28] C. Adamo, V. Barone, Toward reliable density functional methods without adjustable parameters: the PBE0 model, *J. Chem. Phys.* 110 (1999) 6158–6170.
- [29] L. Chen, L. Wang, Y. Wan, Y. Zhang, Z. Qi, X. Wu, H. Xu, Acetylene and diacetylene functionalized covalent triazine frameworks as metal-free photocatalysts for hydrogen peroxide production: a new two-electron water oxidation pathway, *Adv. Mater.* 32 (2020) 1904433.
- [30] F. Michaillodou, N. Klöcker, N.V. Cornelissen, R.K. Singh, A. Peters, A. Ovcharenko, D. Kümmel, A. Rentmeister, Cover picture: engineered SAM synthetases for enzymatic generation of admeton analogs with photocaging groups and reversible DNA modification in cascade reactions, *Angew. Chem. Int. Ed.* 60 (2021), 1–1.
- [31] X. Hu, Z. Zhan, J. Zhang, I. Hussain, B. Tan, Immobilized covalent triazine frameworks films as effective photocatalysts for hydrogen evolution reaction, *Nat. Commun.* 12 (2021) 6596.
- [32] H. Yamakoshi, K. Dodo, A. Palonpon, J. Ando, K. Fujita, S. Kawata, M. Sodeoka, Alkyne-tag Raman imaging for visualization of mobile small molecules in live cells, *J. Am. Chem. Soc.* 134 (2012) 20681–20689.
- [33] M. Liu, Q. Huang, S. Wang, Z. Li, B. Li, S. Jin, B. Tan, Crystalline covalent triazine frameworks by *in situ* oxidation of alcohols to aldehyde monomers, *Angew. Chem. Int. Ed.* 57 (2018) 11968–11972.
- [34] K. Wang, L.-M. Yang, X. Wang, L. Guo, G. Cheng, C. Zhang, S. Jin, B. Tan, A. Cooper, Covalent triazine frameworks via a low-temperature polycondensation approach, *Angew. Chem. Int. Ed.* 56 (2017) 14149–14153.
- [35] M. Liu, K. Jiang, X. Ding, S. Wang, C. Zhang, J. Liu, Z. Zhan, G. Cheng, B. Li, H. Chen, S. Jin, B. Tan, Controlling monomer feeding rate to achieve highly crystalline covalent triazine frameworks, *Adv. Mater.* 31 (2019) 1807865.
- [36] S. Zhang, G. Cheng, L. Guo, N. Wang, B. Tan, S. Jin, Strong-Base-Assisted Synthesis of a Crystalline Covalent Triazine Framework with High Hydrophilicity via Benzylamine Monomer for, in *Angew Photocatalytic Water Splitting* (Ed.), *Chem Int.* 59, 2020, pp. 6007–6014.
- [37] S. Wang, X. Hai, X. Ding, S. Jin, Y. Xiang, P. Wang, B. Jiang, F. Ichihara, M. Oshikiri, X. Meng, Y. Li, W. Matsuda, J. Ma, S. Seki, X. Wang, H. Huang, Y. Wada, H. Chen, J. Ye, Intermolecular cascaded  $\pi$ -conjugation channels for electron delivery powering  $\text{CO}_2$  photoreduction, *Nat. Commun.* 11 (2020) 1149.
- [38] Y. Wu, J. Chen, H. Che, X. Gao, Y. Ao, P. Wang, Boosting 2e– in garland carbon nitride with carbon defects for high-efficient photocatalysis-self-Fenton degradation of 2,4-dichlorophenol, *Appl. Catal. B* 307 (2022), 121185.
- [39] J. Ma, K. Wang, C. Wang, X. Chen, W. Zhu, G. Zhu, W. Yao, Y. Zhu, Photocatalysis-self-Fenton system with high-fluent degradation and high mineralization ability, *Appl. Catal. B* 276 (2020), 119150.
- [40] Z. Teng, N. Yang, H. Lv, S. Wang, M. Hu, C. Wang, D. Wang, G. Wang, Edge-functionalized  $\text{g-C}_3\text{N}_4$  nanosheets as a highly efficient metal-free photocatalyst for safe drinking, *Water Chem.* 5 (2019) 664–680.
- [41] Y. Qian, D. Li, Y. Han, H.-L. Jiang, Photocatalytic molecular oxygen activation by regulating excitonic effects in covalent organic frameworks, *J. Am. Chem. Soc.* 142 (2020) 20763–20771.